ADVANCED MATERIALS
www.advmat.de

Transition of Néel-Type and Bloch-Néel Hybrid Skyrmion in a Metallic Multilayer Material System

Binbin Wang, Núria Bagués, Shuyu Cheng, Shekhar Das, Camelia Selcu, Ziling Li, Jacob B. Freyermuth, Denis V. Pelekhov, P Chris Hammel, Mohit Randeria, Roland K. Kawakami, and David W. McComb**

Magnetic skyrmions, which are stable, topologically protected spin structures, have garnered significant interest for their potential in revolutionizing spintronic applications. This study reveals the room-temperature coexistence of Néel-type and Bloch-Néel hybrid skyrmions in [Pt/Co/Cu] multilayers grown by molecular beam epitaxy (MBE). Pulse current is used to switch the skyrmion type and modulate the stability of the skyrmions. The thermal effect on the stability of the skyrmions due to the current pulse is also investigated. The work unveils a broad magnetic phase space, offering unprecedented control over skyrmion states in metallic multilayers with broken inversion symmetry. These findings pave the way for diverse applications in spintronics, including binary data encoding, and provide a novel framework for the manipulation of multi-type skyrmions.

1. Introduction

Magnetic skyrmions are stable topological spin textures that can occur in certain types of magnetic materials.[1–6] In noncentrosymmetric magnets, three types of skyrmions are often observed, namely Bloch-type, Néel-type, and Bloch-Néel hybrid type,[7,8] while other topological spin textures, like antiskyrmions, may also exist.[1,4] The type of magnetic skyrmion that forms is associated with the symmetry and Dzyalloshinskii–Moriya interactions (DMI) of spin-orbit-coupling (SOC) origin in the host material.[4] For example, Bloch-type skyrmions are mainly found in chiral magnets that have broken inversion symmetry in the crystal, such as B20 compounds and their thin films.[9–12] In contrast, the interfaces in artificial heterostructures, or bulk crystals with broken mirror symmetry, can stabilize Néel-type skyrmions.[13–17] Typically, each material can only host one type of skyrmions, while the coexistence between multiple types of skyrmions in the same sample has only been observed very recently.[7,18]

Controlling and manipulating two or more distinct types of skyrmions in a single system could enable new spintronic phenomena and versatile applications, such as binary data encoding.[7,19–22] Traditionally, binary encoding with skyrmions has relied on modulating chirality. However, we propose a novel approach where binary states are represented by distinct skyrmion types, namely Néel type and Bloch-Néel hybrid type (hereafter "hybrid"), providing an additional degree of freedom for encoding information. This strategy is advantageous for systems where chirality is challenging to manipulate but type differentiation is practical. For example, in racetrack memory devices, Néel and hybrid skyrmions can serve as "0" and "1" states, respectively, with detection achievable using their opposite skyrmion Hall effects.[18]

In this study, using Lorentz transmission electron microscopy (L-TEM) we demonstrate the coexistence of Néel and hybrid skyrmions at room temperature in MBE grown [Pt/Co/Cu] multilayers. Moreover, we show that by biasing a pulse current, it is possible to modulate the stabilization of the skyrmion-type phases. Further results highlight the role of thermal effects in triggering the complex behavior of skyrmions. This contribution opens a new route for nucleating and manipulating multiple types of skyrmions in inversion-symmetry broken magnetic multilayer systems, which could enrich potential applications in spintronic devices.

B. Wang[+], N. Bagués[++], D. W. McComb
Center for Electron Microscopy and Analysis
Ohio State University
Columbus, OH 43212, USA
E-mail: nbagues@cells.es; mccomb.29@osu.edu
B. Wang[+], N. Bagués[++], D. W. McComb
Department of Material Science and Engineering
Ohio State University
Columbus, OH 43210, USA
S. Cheng, S. Das, C. Selcu, Z. Li, J. B. Freyermuth, D. V. Pelekhov, P C. Hammel, M. Randeria, R. K. Kawakami
Department of Physics
The Ohio State University
Columbus, OH 43210, USA

The ORCID identification number(s) for the author(s) of this article can be found under https://doi.org/10.1002/adma.202514228

[+]Present address: Intel Corporation, Hillsboro, OR 97124, USA

[++]Present address: ALBA Synchrotron Light Source,CELLS, Cerdanyola del Vallès 08290, Spain

DOI: 10.1002/adma.202514228

2. Results

2.1. Coexistence of Distinct Skyrmions

$[Pt/Co/Cu]_5$ multilayer specimens are grown on an $Al_2O_3(0001)$ substrate with a Pt(111) buffer layer. High-angle annular dark field (HAADF) and energy-dispersive X-ray (EDX) mapping techniques are used to confirm the layer structure of the samples. In our previous work,[23] we have systematically studied the structural dependence of the magnetic properties of $[Pt/Co/Cu]_5$ multilayers and established the presence of magnetic skyrmions in the samples showing zero-field magnetic multidomain states. In this work, we focus on the samples consisting of five periods of Pt(0.4 nm)/Co(1.2 nm)/Cu(0.45 nm) structures as a representative material in this family (**Figure 1A**; Figure S1, Supporting Information). The magnetic hysteresis loops, as shown in Figure 1B, reveal a dominant perpendicular magnetic anisotropy (PMA) in the magnetic phase evolution. Using L-TEM, a labyrinthine magnetic phase is observed at zero magnetic field that decays into sparse stripes followed by a skyrmion phase with increasing external magnetic field strength (Figure 1C-i–iii). Removing the magnetic field after saturation recovers the initial labyrinth state without an intermediate phase (Figure 1C-iii–v), as evidenced in the bump curve in Figure 1B, suggesting a rapid shift from a polarized to a multidomain state. The sheared hysteresis loop suggests that the transitions between magnetic states are contingent upon their initial states, a phenomenon also reported in similar material systems.[8,24–26]

Recent theoretical predictions suggest the possible existence of room-temperature ferromagnet (FM)-/antiferromagnet (AFM)-coupled skyrmions in Pt/Co/Z systems (Z = Pd, Cu, Ag, Au, Zn, and Cd) due to PMA and interfacial DMI.[8,27] Although a Néel-type configuration is expected for an interfacial DMI system, we observe the coexistence of both Néel and hybrid skyrmions in Figure 1C-iii.[28] Their magnetic signatures are distinguishable through contrast variations in L-TEM images under stronger magnetic fields (Figure S2, Supporting Information), with line profiles in Figure 1D indicating unique topological features and uniform sizes of ≈100 nm.[8,29] In defocused L-TEM, skyrmions comprising of Bloch character manifest along the electron beam without sample tilting, forming closed loops in the projected in-plane induction field that affect the electron beam convergence, rendering them visible as phase objects. The opposite contrast of the Bloch-type skyrmion-like textures suggests that their chirality can be of either sign. In contrast, Néel-type skyrmions, imperceptible through direct phase contrast, are made visible by tilting the sample, which yields a contrast from the oppositely polarized field at their core and periphery. This results in a characteristic dark and bright paired contrast in L-TEM images. The reconstructed phase and magnetic induction maps from defocused image series at a 14-degree tilt (Figure 1E) concur with simulated phase images (Figure S7, Supporting Information), differentiating the Néel-type skyrmions by their combination of clockwise and counterclockwise spin curls, and hybrid skyrmions by singular spin curls in the induction field map.[30] These observations align with our L-TEM simulation presented in Figure S7 (Supporting Information), which is based on the subsequent micromagnetic simulation.

The appearance of skyrmions with Bloch character in this material system is rather surprising because of its microscopic origin that remains an open question, since it is usually induced by the Dresselhaus SOC[6] while some topologically similar spin structures can be dipolar stabilized.[4,31,32] One possibility is the competition between the anisotropic symmetric exchange and antisymmetric exchange by considering both the SOC and the spin-charge coupling, as predicted in a recent theoretical work.[33] On the other hand, recent theoretical studies have shown that there might be no interfacial DMI at the Co/Cu interface while the effective DMI is from the Pt/Co interface when these two layers can be treated as independent (provided that Co is thicker than 3 MLs).[27,34] Since the Co/Cu/Pt system consists of multilayers with specifically tailored magnetic properties, small changes in the properties of individual layers have the potential to affect the competition for exchange and DMI energy. For example, skyrmion-like structures with opposite Bloch components have been reported in Pd/Co bilayer systems, while no Néel-type skyrmion has been reported.[8]

2.2. Current-Driven Stabilization of Distinct Skyrmion Phases

To study the stability of the skyrmions and their dynamics under bias currents, the multilayer film is mounted on a commercial biasing chip that is connected to an external bias system (see Methods). To achieve electron transparency, the substrate is back-thinned to avoid FIB beam damage to the active layers, as shown in **Figure 2A**. A thickness gradient is created intentionally to produce a thermal gradient along the channel because aluminum oxide is an insulator. Therefore, the thicker substrate will cool down the [Pt/Co/Cu] layers faster by absorbing Joule heat generated by the bias current. The relative thickness of the substrate can be observed by the relative change in the Al and Co EDX signals, as shown in Figure 2B.

Figure 2C shows the transition in the skyrmion phase within the same region of the sample after two 100 ns pulses. Before applying the current pulses, the initial state is a mixture of hybrid and Néel skyrmions at 100 mT, as discussed in Figure 1. After a pulse of 2.6×10^{11} A m^{-2}, some Néel-type skyrmions nucleated in this region, while hybrid skyrmions still survived and even a new particle-like magnetic texture was nucleated. However, after a current pulse with a higher current density of 5.1×10^{11} A m^{-2}, most hybrid skyrmions are annihilated and replaced by Néel-type skyrmions. This phase change reflects a collective reconstruction of the local magnetization texture rather than a direct transformation of individual skyrmions. Due to the substrate thickness gradient, as shown in Figure 2B, a dense state of Néel-type skyrmions appears more prevalently in thinner substrate regions, where the temperature is higher under the bias current pulse. This trend is further confirmed by varying the biasing current pulse width, as shown in Figure S3 (Supporting Information). We find that at the same magnetic field, wide current pulses lead to more nucleation events of skyrmions, suggesting that the skyrmions are nucleated by thermal effect, which also agrees with the previous studies.[24,26,35–37]

The transition from a sparse hybrid skyrmion state to a dense Néel skyrmion lattice state is reminiscent of a similar transition observed in $Fe_{3-\delta}GeTe_2$ flakes, where Néel (Bloch) skyrmion

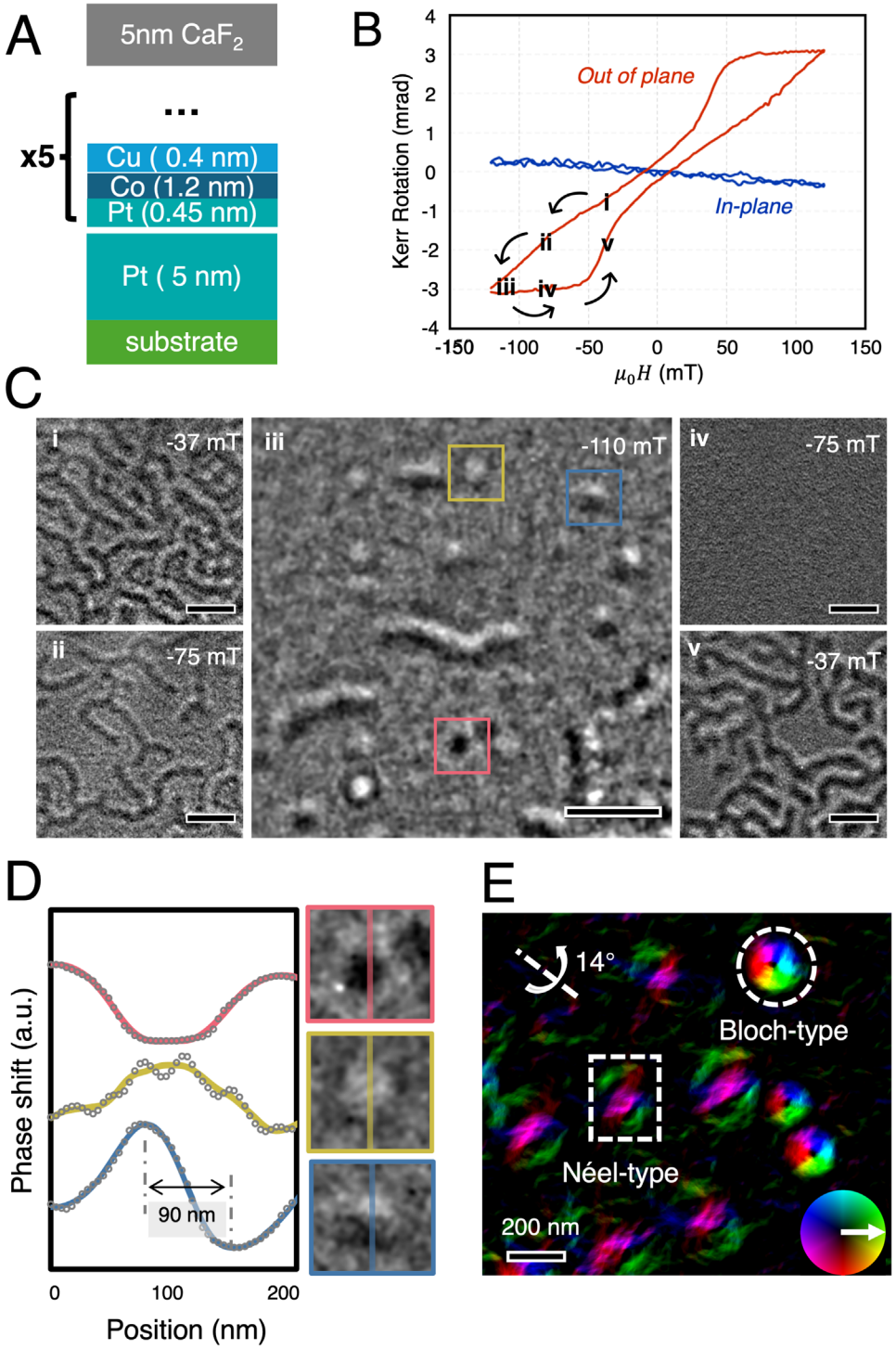

Figure 1. Magnetic field dependence of magnetic phase transitions and coexistence of different types of skyrmions in a $[Pt/Co/Cu]_5$ multilayer at room temperature. A) Schematic diagram of a typical cross-section of a multilayer thin film. B) Magnetic hysteresis loops measured with magneto-optical Kerr effect (MOKE) along the in-plane and out-of-plane directions. C) L-TEM images of the same region under different magnetic fields, with magnetic fields applied in the order shown in (B). Scale bar is 500 nm. D) Line profiles of different types of skyrmion observed in (C). E) The projected magnetic induction field mapping of a coexistence of different types of skyrmions at 120 mT (see methods). The color and arrows indicate induction field components perpendicular to the beam propagation direction.

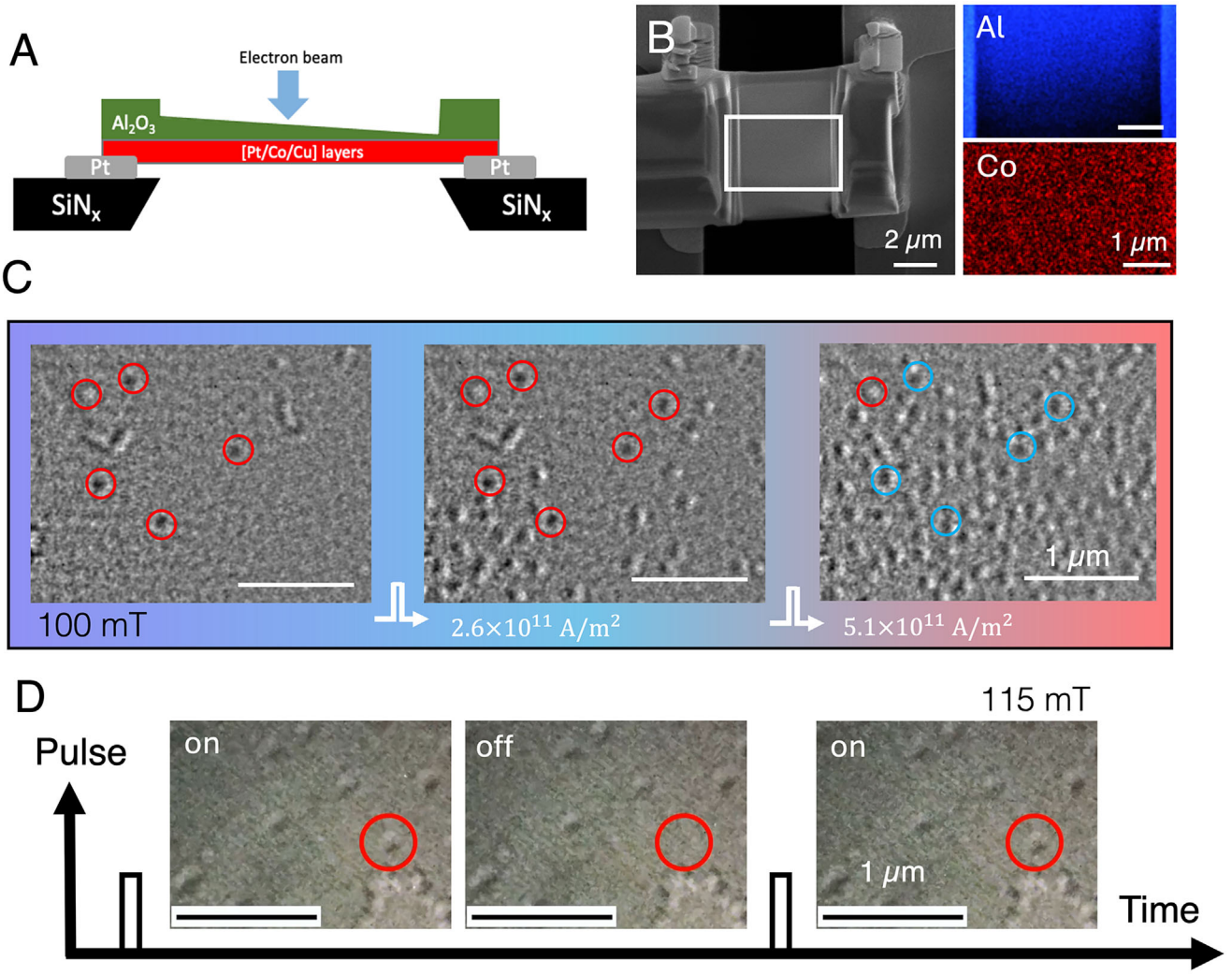

Figure 2. Thermal-driven phase transition of skyrmion states under biasing currents. A) Schematic of the device cross-section. B) Device configuration from electron beam view, where the EDX mapping of Al and Co indicates a thickness gradient from the substrate side (Al_2O_3). C) Collective phase transition of skyrmion states after applying 100 ns current pulses. The region transitions from a mixed Bloch- and Néel-type skyrmion phase to a Néel-dominated phase, with increasing skyrmion density due to thermal effects. Red circles highlight Bloch-type skyrmions, while blue circles indicate areas of transition to Néel-type. Note the substrate thickness gradient from top (thicker) to bottom (thinner), influencing local temperature. D) A single skyrmion "on" and "off" after a biasing current of 150 ns at 2.5×10^{11} A m^{-2}.

lattices are observed for thinner (thicker) samples.[38] In $Fe_{3-\delta}GeTe_2$, the thickness-induced transition is explained by thinner flakes having weaker dipolar interaction and therefore favoring Néel skyrmion lattices. Meanwhile, the simulation results in the same work exhibit a general trend of increased skyrmion density as PMA reduces. In our case, the current pulses heat up the sample, causing the saturation magnetization M to reduce (see Figure S11, Supporting Information for the M vs T curve). As a result, both dipolar interaction and PMA are expected to reduce.[39] This makes the high-density Néel skyrmion lattice state more energetically favorable over the sparse Bloch skyrmion state. Such a picture is further evidenced by increasing the temperature of the film by DC current, which stabilizes the Néel-type skyrmion in a dense state (Figure S12, Supporting Information). Meanwhile, hybrid skyrmions are also present when DC current is applied (Figure S13, Supporting Information), and the transition occurs only when stimulated by a short current pulse. This can be explained by the existence of an energy barrier between the sparse hybrid skyrmion state and the dense Néel skyrmion lattice state. Application of pulsed current overcomes this energy barrier and brings the system to the more energetically favorable state.

Here, we note that the explanation above does not exclude other possible mechanisms, like spin transfer and/or spin-orbit torque. Moreover, local structural properties should also play a role in the nucleation of skyrmions in this multilayer material system (Text S2, Figure S8–S10, Supporting Information). As shown in Figure 2D and Movie S1 (Supporting Information), a single Néel-type skyrmion is stimulated to nucleate by a current pulse of 150 ns and then stabilizes ("on") for a few seconds before annihilating ("off"). This switching of the "on" and "off" states can be controlled by short current pulses. More importantly, the observation that skyrmion is pinned at a specific location

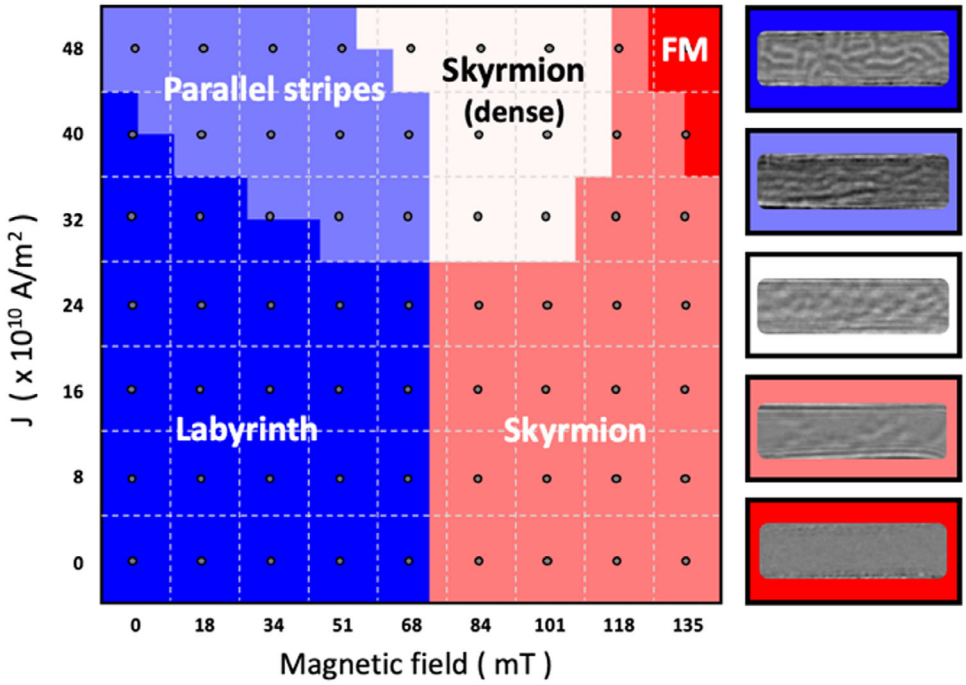

Figure 3. Magnetic phase diagram of current density and magnetic field dependence. Increasing bias currents are applied to the magnetic phases at different magnetic fields with a current pulse width of 100 ns. The various magnetic phases are distinguished by different colors, as shown on the right. For consistency, the magnetic phases are initialized to zero field after the hysteresis loop, before applying the increased current pulse.

suggests the role of bias pulse currents and local inhomogeneous coupling, while the underlying mechanisms need to be studied more systematically in combination with multiple characterization techniques and microelectromagnetic simulations.

2.3. Biasing the Current Stabilized Magnetic Phase Diagram

Our results enable the construction of the current-dependent magnetic phase diagram of the material system (**Figure 3**). Starting from a labyrinthine state at zero magnetic field (after a demagnetization process), the magnetic field is then raised to a specific range before a short current pulse of 100 ns is applied. At low magnetic fields, the labyrinth phase stabilizes until it undergoes a transition to a parallel stripe shape at a current pulse density greater than $\approx 2.4 \times 10^{11}$ A m^{-2}. Figure S14 (Supporting Information) shows an example of the transition from the labyrinth phase to the parallel stripe phase. The stripes are Néel-type because they are only observed when the sample is tilted, as discussed in Figure 1, while the labyrinth phase should be a mixture of Néel- and Bloch-type magnetic domains in nature. It is also observed that the stripe phase is parallel to the current direction, suggesting a possible role of spin transfer and/or spin-orbit torque in addition to the thermal effect caused by the bias current. Increasing the magnetic field, the labyrinth transforms into a sparse skyrmion phase when the bias current is low, while short bias current pulses can help stabilize the dense skyrmion phase, which has been reported to be more energetically advantageous than the sparse skyrmion phase in a moderate magnetic field range.[24] Since there is no existence of stripe domains at the initial status of the spare skyrmion phase and no unidirectional motion of skyrmion is observed, the additional skyrmions should be thermally nucleated as a consequence of the biasing current pulse.[40]

2.4. Micromagnetic Simulations

To understand the coexistence of Néel skyrmions and hybrid skyrmions in Pt/Co/Cu multilayers, we perform micromagnetic simulations using MuMax3[41] (see Experimental Section). Starting from a Néel skyrmion with ≈75 nm diameter as the initial state, the system relaxes into a Néel skyrmion state (**Figure 4A**). This is better visualized by the x-component of magnetization m_x, as shown in the right panel of Figure 4A. The m_x features a positive lobe on the left side and a negative lobe on the right side, which is expected for Néel skyrmions. In contrast, if the system relaxes from a Bloch skyrmion with ≈75 nm diameter as the initial state, the final state will be a Néel-Bloch hybrid state (hereafter "hybrid skyrmion") displayed in Figure 4B. The m_x shows a maximum at the top but slightly toward left, while the minimum of m_x shows up at the bottom but slightly toward right, as shown in the right panel of Figure 4B. This indicates that this hybrid state is closer to a Bloch skyrmion but still comprises Néel characters. For both Néel and hybrid skyrmions, there is no variation in magnetization textures from the top layer to the bottom layer of Co, due to the exchange interaction between neighboring Co layers. The Néel skyrmion has a slightly lower total energy (−3.73 kJ m^{-3} referenced to an out-of-plane magnetized state) than the hybrid skyrmion (−3.71 kJ m^{-3}), and the energy barrier between these two states is estimated to be below −0.07 kJ m^{-3} (see Text S1 and Figure S6, Supporting Information). This value is

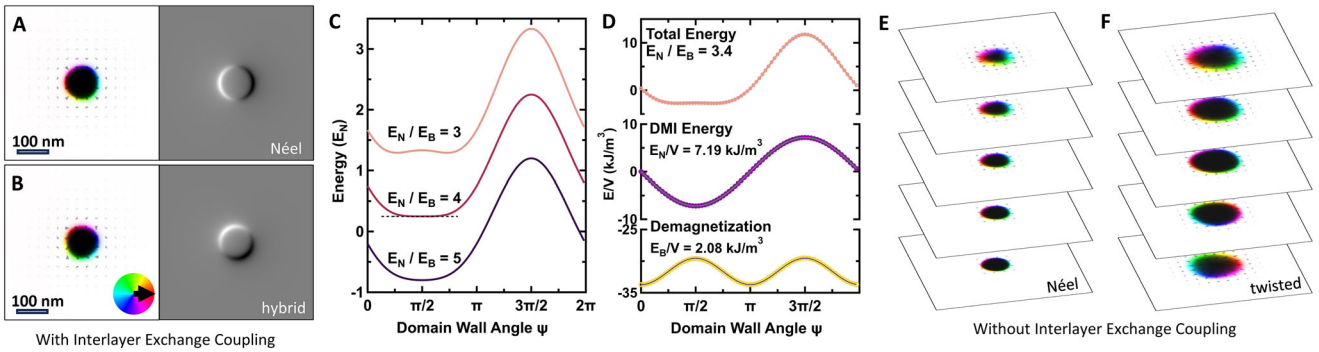

Figure 4. Micromagnetic simulation of skyrmions in [Pt/Co/Cu] multilayers. A,B) Simulations with interlayer exchange coupling turned on. A) The final state relaxed from a Néel skyrmion to the initial state. B) The final state relaxed from a Bloch skyrmion as the initial state. The left panels of (A) and (B) show all three components of magnetization, while the right panels only show the x-component of magnetization. The insect of (B) shows the color map, which represents the in-plane component of magnetization directions. C) Domain wall angle (ψ) dependence of the total energy with $E_N/E_B = 3$ (top), 4 (middle), and 5 (bottom), respectively. The black dashed line is the guide to the eye. D) Total energy (top), DMI energy (middle), and demagnetization energy (bottom) of the ansatz series with different domain wall angle ψ. The solid lines are the fitting results with $-\sin\psi$ and $-\cos 2\psi$, respectively. The energies are referenced to an out-of-plane magnetized state and are normalized to the volume of the system. E,F) Simulations with interlayer exchange coupling turned off. (E) is relaxed from a Néel skyrmion while (F) is relaxed from a Bloch skyrmion.

comparable to previously reported simulations of the energy differences between distinct spin textures at their local energy minima.[26]

The coexistence of Néel skyrmions and hybrid skyrmions can be understood using a phenomenological model as follows. The skyrmions stabilized in our simulations can be viewed as "magnetic domain wall skyrmions,"[42] which have an inverted magnetic domain in the center surrounded by a chiral domain wall whose width is much smaller than the diameter of the inverted domain. Therefore, we use the following domain wall profile as an ansatz,[42,43] expressed in cylindrical coordinates with the origin at the skyrmion center:

$$m_r = -\sin\psi / \cosh\left(\frac{r-q}{\Delta}\right), m_\phi = \cos\psi / \cosh\left(\frac{r-q}{\Delta}\right),$$
$$m_z = \tanh\left(\frac{r-q}{\Delta}\right) \quad (1)$$

where ψ is the "domain wall angle" defined with respect to the tangential direction (see Figure S4, Supporting Information), Δ is the domain wall width, q is the diameter of the skyrmion, and r is the distance to the center of the skyrmion. The introduction of the "domain wall angle" ψ allows one to quantify the mixing ratio between Bloch skyrmions and Néel skyrmions, where $\psi = 0$ or π corresponds to Bloch skyrmions, and $\psi = \frac{\pi}{2}$ or $\frac{3\pi}{2}$ correspond to Néel skyrmions with opposite chirality, respectively. Fitting the linecut profiles of the Néel (hybrid) skyrmion yields the skyrmion radius and domain wall width of 54.8 nm (52.7 nm) and 6.2 nm (7.4 nm), respectively (see Figure S5, Supporting Information).

Stabilization of the skyrmion is the outcome of competition between multiple energy terms, including magnetic anisotropy, Zeeman energy, exchange interaction, DMI, and demagnetization energy, etc. We first consider the ψ dependence of the total energy on the lowest order. The energy term favoring Bloch skyrmions (labeled as E_B) should have the $-\cos 2\psi$ dependence to have minima at 0 or π. Similarly, the energy term favoring Néel skyrmions (labeled as E_N) should follow $-\sin\psi$, which has its minima at $\psi = \frac{\pi}{2}$. Therefore, the total energy can be written as:

$$E_{total} = -E_B \cos 2\psi - E_N \sin\psi \quad (2)$$

Phenomenologically, whether Néel or hybrid skyrmion being the ground states depends on the competition between E_B and E_N. When $E_N > 4E_B$, the total energy has a single minimal at $\psi = \frac{\pi}{2}$, which corresponds to a Néel skyrmion state (Figure 4C, bottom). On the other hand, when $E_N < 4E_B$, the total energy has two minima symmetric about $\psi = \frac{\pi}{2}$, which corresponds to a hybrid skyrmion state (Figure 4C, top). In between these two cases, a critical point occurs at $E_N = 4E_B$, where the energy barely varies within a wide range around $\psi = \frac{\pi}{2}$ (Figure 4C, middle). Our system is likely to fall around this critical point, where Néel skyrmions and hybrid skyrmions are close in energy.

To verify the aforementioned hypothesis, we initialize a series of domain wall skyrmions ansatzes with domain wall angles varying from 0 to 2π. The radius and domain wall width are set to be 53.8 and 6.8 nm, respectively, which are the average values of the Néel and hybrid skyrmions. By examining the ψ dependence of individual energy terms, we find that the DMI energy follows the $\sin\psi$ relationship while the demagnetization energy shows a $\cos 2\psi$ relationship with a constant background, as shown in Figure 4D. All other energy terms (magnetic anisotropy, exchange interaction, and Zeeman energy) do not show any ψ dependence. This establishes the competition between DMI and demagnetization energy as the primary driving factor for the coexistence between Néel and hybrid skyrmions. By fitting the ψ-dependent components of DMI and demagnetization energies, we are able to obtain E_N (E_B) of 7.19 kJ m^{-3} (2.08 kJ m^{-3}). The ratio $\frac{E_N}{E_B} = 3.4$ indicates that this ansatz series is indeed close to the critical point, with a hybrid skyrmion being the ground state (see Figure 4D). The Néel skyrmion is only 0.07 kJ m^{-3} less energetically favorable than the hybrid skyrmion. In particular, the hybrid skyrmion as the ground state reflects the intrinsic tendency of the

Table 1. Comparison between Néel and hybrid skyrmions. All energy density ε terms are referenced to an out-of-plane magnetized state and are normalized by the volume of the system.

	Radius q [nm]	DW width Δ [nm]	ε_{DMI} [J m^{-3}]	ε_{demag} [J m^{-3}]	ε_{ani} [J m^{-3}]	ε_{exch} [J m^{-3}]	ε_{Zeeman} [J m^{-3}]	ε_{total} [J m^{-3}]
Néel	54.8	6.2	−73.63	−351.22	254.55	42.17	90.88	−37.26
Hybrid	52.7	7.4	−48.69	−370.07	265.13	31.96	84.60	−37.07
$\varepsilon_{Néel} - \varepsilon_{Hybrid}$	-	-	−24.94	18.85	−10.58	10.21	6.27	−0.19

system to form a vortex state in order to minimize depolarization energy, even in the absence of DMI.[44,45]

While the lowest-order phenomenological theory suggests that the system is close to the critical point, it only allows one type of skyrmion to become the local energy minima. Also, calculation results from the ansatz series imply hybrid state being the energy minima, contradicting our simulation results that the Néel skyrmion is slightly energetically favorable than the hybrid skyrmion. To solve this paradox, we closely examine individual energy terms summarized in **Table 1**. In addition to the DMI energy, we find that the magnetic anisotropy also contributes to the stabilization of the Néel skyrmion. This is attributed to the smaller domain wall width of the Néel skyrmion, which leads to less in-plane component of spins. The smaller domain wall width of the Néel skyrmion can be understood by considering the analytical solution of the domain wall width:[46]

$$\Delta = \sqrt{\frac{A}{K_u - \frac{1}{2}\mu_0 M_S^2 N}} \tag{3}$$

where A is exchange stiffness, K_u is the uniaxial anisotropy, and the factor N is related to the demagnetization effects. Since the demagnetization energy is reduced for the Néel skyrmion, the effective anisotropy $K_u - \frac{1}{2}\mu_0 M_S^2 N$ is expected to increase. Therefore, the domain wall width for the Néel skyrmion becomes smaller, which in turn reduces the anisotropy energy and contributes to the E_N term in Equation (2). This mechanism may add higher-order terms to Equation (2), enabling the presence of one additional local energy minima at $\psi = \frac{\pi}{2}$ which corresponds to the Néel skyrmion state.

Interlayer exchange coupling between neighboring Co layers also plays an important role in stabilizing both types of skyrmions. Figure 4E,F display the simulation results with interlayer exchange coupling turned off, i.e., the neighboring Co layers are only coupled through magnetic dipolar interaction. When a Néel skyrmion is used as the initial state, the final state remains a Néel-type skyrmion in each Co layer (Figure 4E), with the width of the "domain wall" region becoming wider from bottom to top. The skyrmion has the same chirality through all five layers, i.e., the spins tumble outward. On the other hand, when the system is relaxed from a Bloch skyrmion, the final state is a "twisted" skyrmion (Figure 4F), where a Néel skyrmion in the bottom layer evolves into a hybrid skyrmion in the second from bottom layer and then evolves into a Néel skyrmion with opposite chirality for the top three layers. A similar simulation result has also been reported by Lemesh et al.[43] The reason for twisted skyrmion formation is that twisting the domain wall from Néel-type to Bloch-type, then to Néel-type with opposite chirality, helps to minimize the demagnetizing energy. Meanwhile, the introduction of DMI breaks the symmetry of the Néel-type walls with opposite chirality, and thus shifts the Bloch layer up and down. Here, we note that the strength of the interlayer exchange interaction is set to be 10% of the intralayer exchange coupling, and it only couples the neighboring Co layers. Therefore, the energy scale of interlayer exchange interaction is estimated to be less than 5% of the total exchange interaction, and one or two orders of magnitude smaller than other energy scales. However, our simulation suggests that such a small energy scale is crucial in maintaining the same skyrmion profile across the entire sample and therefore cannot be ignored when considering the interactions that stabilize both Néel and hybrid skyrmions.

3. Conclusion

In this study, we have successfully shown that both hybrid and Néel-type skyrmions can coexist in metallic multilayer systems. The application of short bias currents enabled us to observe real-time, location-specific transitions between these skyrmion types. While direct transformations of individual skyrmions have not been observed, these transitions can be attributed to various factors, including local structural variations, thermal effects induced by the biasing current, and influences of spin-transfer and orbital torque. This approach highlights the role of thermal gradients and local non-uniformities in manipulating skyrmion behavior. Our findings provide a pathway for using skyrmion types as binary states in data encoding applications. By selectively stabilizing hybrid or Néel-type skyrmions through controlled current pulses, we introduce an additional degree of freedom for information storage, moving beyond chirality-based schemes. This capability expands the potential for multi-type skyrmion platforms in spintronic devices (see Figure S15, Supporting Information for a proposed device scheme). Furthermore, our work uncovers an expansive magnetic phase space and shed lights on competing energy scales in stabilizing skyrmions in a multilayer system. These findings may serve as guidelines for designing skyrmion materials in the future and facilitate unprecedented control over skyrmion behavior through the manipulation of variables such as layer thickness, structural periodicity, and current parameters. Collectively, this work opens novel pathways for the theoretical and empirical investigation of skyrmions and lays the groundwork for future advancements in skyrmionics.

4. Experimental Section

Sample Preparation: $[Pt/Co/Cu]_5$ multilayer specimens are epitaxy grown on Al_2O_3 (0001) substrate with Pt(111) buffer layer using MBE. Prior to the growth of multilayers, a 5 nm epitaxial Pt(111) buffer layer is grown on the Al_2O_3 (0001) substrate by depositing a 0.7 nm nucleation layer at T = 450 ^{0}C, then depositing a 4.3 nm continuation layer while naturally cooling down from T = 140 ^{0}C. The Pt(111) buffer layer is subsequently annealed at T = 300 ^{0}C for 10 min to improve the crystallinity, then cooled down to room temperature. The Pt/Co/Cu multilayers are then epitaxially grown on top of Pt(111) buffer layer at room temperature by sequentially opening the computer-controlled shutters in front of Co, Cu, and Pt evaporation cells. The growth rate of the individual layer is measured by a quartz crystal monitor before the growth. A 5 nm CaF_2 capping layer is used to prevent the sample from oxidation. The detailed structural and magnetic characterizations of [Pt/Co/Cu] multilayers are presented in our previous work.[23]

HAADF scanning (S)TEM imaging and EDX analysis are performed to characterize the structure and quality of the films in cross-section specimens using a probe-corrected Themis Z S/TEM at 300 kV, equipped with a Super-X detector. Cross-section samples are prepared using a focused ion beam (FIB) instrument. Plan view (PV) specimens to study magnetic phases, skyrmion type and transition, and pinning effects are prepared from the cleaving edge of the specimens, also using FIB. To conduct biasing experiments, PV specimens are mounted and directly thinned on biasing nano-chips compatible with an in situ TEM holder (DENS wildfire/lightning). STEM-EDX analysis from PV specimens is performed using an image-corrected Titan 60–300 S/TEM at 300 kV, equipped with a Super-X detector.

Magnetic Imaging: Magnetic imaging is conducted using the Fresnel mode of Lorentz imaging in an image-corrected Titan 60–300 S/TEM at 300 kV. The objective lens of the microscope is adjusted to modify the magnetic field conditions at the sample position. The technique utilizes large defocus values, typically in the range of hundreds of micrometers to 1 mm, to reveal the contrast of magnetic domain walls in the intensity distribution. The presence of a rotating magnetic field in Bloch-type and Néel-type skyrmions results in a variation in intensity, depending on the helicity and sign of the defocus. To image Néel-type magnetic structures, tilt angles of samples are applied in a range of 15–25 degree. In addition, the background subtraction method is implemented to provide a qualitative image of the weak magnetic phase contrast and remove unwanted background signal, following reference.[11] Projected magnetic induction field maps are reconstructed from defocus series images of 500 µm at 14 degree tilt using an open-sourced script based on the transport of intensity equation.[47]

Micromagnetic Simulations: Micromagnetic simulations are performed on a slab consisting of 256×256×48 cells using MuMax3.[41] The size of each cell is $2 \times 2 \times 0.2$ nm^3, and each layer in the vertical direction represents one atomic layer. The micromagnetic parameters used are saturation magnetization of Co $M_{Co} = 1.4 \times 10^3$ kA m^{-1}, saturation magnetization of Pt $M_{Pt} = 1.7 \times 10^3$ kA m^{-1}, intralayer exchange stiffness A_{ex} = 25 pJ m^{-1}, uniaxial anisotropy K_u = 1.6 mJ m^{-2}, and interfacial DMI value D = 2.15 mJ m^{-2}. The strength of the interlayer exchange interaction between neighboring Co layers is set to 10% of the intralayer exchange coupling within a single Co layer. The selection of these values has been justified in our previous work.[23] Using these parameters, we are able to reproduce the major magnetic properties of Pt/Co/Cu multilayers, including out-of-plane single domain to multidomain transition at zero field with increasing number of periods N, the width of magnetic stripe domains at zero field, and the size of skyrmions. The applied field in our micromagnetic simulation is kept at 100 mT along the out-of-plane direction. Runge-Kutta solvers of orders two and three (rk23) are used in all our simulations.

The L-TEM simulation for skyrmions is conducted on the micromagnetic simulation at various tilt angles using PyLorentz.[48]

In Situ Setting: In situ magnetic fields or/and biasing are applied to $[Pt/Co/Cu]_5$ magnetic multilayer specimens using L-TEM mode and a DENS wildfire/lightning holder. We have implemented a high-frequency circuit with the existing DENS sample holder. The sample holder itself is not designed for a high-frequency application. However, we have utilized the low-frequency wires coming from the sample space (≈2 m long) in a particular combination so that the hot lead stays close to the ground lead. The sample holder ends with a LEMO connector. We prepared a LEMO to SMA/BNC adapter to connect to the high voltage pulser (Berkeley Nucleonics, Model 577) and the oscilloscope (Tektronix, TDS 3054B). A representative transmitted voltage pulse is shown in Figure S16 (Supporting Information).

Supporting Information

Supporting Information is available from the Wiley Online Library or from the author.

Acknowledgements

B.W. thanks the support from Presidential Fellowship of the Ohio State University. P.C.H., M.R., R.K.K., and D.W.M. acknowledges partial support from the Center of Emergent Materials, an NSF MRSEC, under award number DMR-2011876. Electron microscopy experiments were supported by the Center for Electron Microscopy and Analysis at the Ohio State University. Defense Advanced Research Projects Agency grant No. D18AP00008.

Conflict of Interest

The authors declare no conflict of interest.

Author Contributions

B.W., N.B., S.C., and S.D. contributed equally to this work. R.K.K., D.W.M., M.R., and P.C.H. performed conceptualization. All authors performed the data curation. S.C., J.B.F., M.R., and R.K.K. performed formal analysis. S.C. performed an investigation (materials synthesis, MOKE). B.W. and N.B. (structural characterization, STEM, EDX, TEM sample preparation). B.W., NB., and S.D. (in situ setup, L-TEM measurements). S.C., B.W., N.B., and S.D. performed methodology. S.C., J.B.F., M.R., R.K.K. (micromagnetic simulations). Software. All authors wrote the original draft. All authors wrote, reviewed, and edited. R.K.K., D.W.M., M.R. and, P.C.H. supervision.

Data Availability Statement

The data that support the findings of this study are available in the supplementary material of this article.

Keywords

Lorentz transmission electron microscopy, metallic multilayer, skyrmions

Received: July 24, 2025
Revised: October 7, 2025
Published online: October 17, 2025

[1] N. Nagaosa, Y. Tokura, *Nat. Nanotechnol.* **2013**, *8*, 899.
[2] R. Wiesendanger, *Nat. Rev. Mater.* **2016**, *1*, 16044.
[3] C. Back, V. Cros, H. Ebert, K. Everschor-Sitte, A. Fert, M. Garst, T. Ma, S. Mankovsky, T. L. Monchesky, M. Mostovoy, N. Nagaosa, S. S. P. Parkin, C. Pfleiderer, N. Reyren, A. Rosch, Y. Taguchi, Y. Tokura, K. Von Bergmann, J. Zang, *J. Phys. D: Appl. Phys.* **2020**, *53*, 363001.

[4] Y. Tokura, N. Kanazawa, *Chem. Rev.* **2021**, *121*, 2857.
[5] W. Jiang, G. Chen, K. Liu, J. Zang, S. G. E. te Velthuis, A. Hoffmann, *Phys. Rep*. **2017**, *704*, 1.
[6] J. Rowland, S. Banerjee, M. Randeria, *Phys. Rev. B* **2016**, *93*, 020404.
[7] X. Lv, H. Lv, Y. Huang, R. Zhang, G. Qin, Y. Dong, M. Liu, K. Pei, G. Cao, J. Zhang, Y. Lai, R. Che, *Nat. Commun.* **2024**, *15*, 3278.
[8] J. A. Garlow, S. D. Pollard, M. Beleggia, T. Dutta, H. Yang, Y. Zhu, *Phys. Rev. Lett.* **2019**, *122*, 237201.
[9] S. Mühlbauer, B. Binz, F. Jonietz, C. Pfleiderer, A. Rosch, A. Neubauer, R. Georgii, P. Böni, *Science* **2009**, *323*, 915.
[10] X. Z. Yu, N. Kanazawa, Y. Onose, K. Kimoto, W. Z. Zhang, S. Ishiwata, Y. Matsui, Y. Tokura, *Nat. Mater.* **2011**, *10*, 106.
[11] B. Wang, N. Bagués, T. Liu, R. K. Kawakami, D. W. McComb, *Ultramicroscopy* **2021**, *232*, 113395.
[12] T. Liu, C. M. Selcu, B. Wang, N. Bagués, P.-K. Wu, T. Q. Hartnett, S. Cheng, D. Pelekhov, R. A. Bennett, J. P. Corbett, J. R. Repicky, B. McCullian, P. C. Hammel, J. A. Gupta, M. Randeria, P. V. Balachandran, D. W. McComb, R. K. Kawakami, *Commun. Phys.* **2023**, *6*, 327.
[13] S. Heinze, K. Von Bergmann, M. Menzel, J. Brede, A. Kubetzka, R. Wiesendanger, G. Bihlmayer, S. Blügel, *Nat. Phys.* **2011**, *7*, 713.
[14] I. Kezsmarki, S. Bordacs, P. Milde, E. Neuber, L. M. Eng, J. S. White, H. M. Rønnow, C. D. Dewhurst, M. Mochizuki, K. Yanai, H. Nakamura, D. Ehlers, V. Tsurkan, A. Loidl, *Nat. Mater.* **2015**, *14*, 1116.
[15] C. Moreau-Luchaire, C. Moutafis, N. Reyren, J. Sampaio, C. A. F. Vaz, N. Van Horne, K. Bouzehouane, K. Garcia, C. Deranlot, P. Warnicke, P. Wohlhüter, J. M. George, M. Weigand, J. Raabe, V. Cros, A. Fert, *Nat. Nanotechnol.* **2016**, *11*, 444.
[16] J. Matsuno, N. Ogawa, K. Yasuda, F. Kagawa, W. Koshibae, N. Nagaosa, Y. Tokura, M. Kawasaki, *Sci. Adv.* **2016**, *2*, 1600304.
[17] A. J. Lee, A. S. Ahmed, J. Flores, S. Guo, B. Wang, N. Bagués, D. W. Mccomb, F. Yang, *Phys. Rev. Lett.* **2020**, *124*, 107201.
[18] B. Dai, D. Wu, S. A. Razavi, S. Xu, H. He, Q. Shu, M. Jackson, F. Mahfouzi, H. Huang, Q. Pan, Y. Cheng, T. Qu, T. Wang, L. Tai, K. Wong, N. Kioussis, K. L. Wang, *Sci. Adv.* **2023**, *9*, ade6836.
[19] F. Zheng, F. N. Rybakov, A. B. Borisov, D. Song, S. Wang, Z. A. Li, H. Du, N. S. Kiselev, J. Caron, A. Kovács, M. Tian, Y. Zhang, S. Blügel, R. E. Dunin-Borkowski, *Nat. Nanotechnol.* **2018**, *13*, 451.
[20] N. S. Kiselev, A. N. Bogdanov, R. Schäfer, U. K. Röler, *J. Phys. D: Appl. Phys.* **2011**, *44*, 392001.
[21] L. Peng, R. Takagi, W. Koshibae, K. Shibata, K. Nakajima, T. hisa Arima, N. Nagaosa, S. Seki, X. Yu, Y. Tokura, *Nat. Res.* **2020**, *15*, 181.
[22] A. O. Mandru, O. Yıldırım, R. Tomasello, P. Heistracher, M. Penedo, A. Giordano, D. Suess, G. Finocchio, H. J. Hug, *Nat. Commun.* **2020**, *11*, 6365.
[23] S. Cheng, N. Bagués, C. M. Selcu, J. B. Freyermuth, Z. Li, B. Wang, S. Das, P. C. Hammel, M. Randeria, D. W. McComb, R. K. Kawakami, *Phys. Rev. B* **2023**, *108*, 174433.
[24] A. M. Park, Z. Chen, X. S. Zhang, L. Zhu, D. A. Muller, G. D. Fuchs, *J. Appl. Phys* **2020**, *128*, 233902.
[25] M. He, L. Peng, Z. Zhu, G. Li, J. Cai, J. Li, H. Wei, L. Gu, S. Wang, T. Zhao, B. Shen, Y. Zhang, *Appl. Phys. Lett.* **2017**, *111*, 202403.
[26] I. Lemesh, K. Litzius, M. Böttcher, P. Bassirian, N. Kerber, D. Heinze, J. Zázvorka, F. Büttner, L. Caretta, M. Mann, M. Weigand, S. Finizio, J. Raabe, M.-Y. Y. Im, H. Stoll, G. Schütz, B. Dupé, M. Kläui, G. S. D. D. Beach, *Adv. Mater.* **2018**, *30*, 1805461.
[27] H. Jia, B. Zimmermann, M. Hoffmann, M. Sallermann, G. Bihlmayer, S. Blügel, *Phys. Rev. Mater.* **2020**, *4*, 094407.
[28] N. Bagues, B. Wang, S. Cheng, D. Das, Z. Li, J. Freyermuth, C. Selcu, D. V. Pelekhov, C. Hammel, M. Randeria, R. Kawakami, D. W. Mccomb, *BIO Web Conf.* **2024**, *129*, 2929019.
[29] S. Pöllath, T. Lin, N. Lei, W. Zhao, J. Zweck, C. H. Back, *Ultramicroscopy* **2020**, *212*, 112973.
[30] T. Denneulin, J. Caron, M. Hoffmann, M. Lin, H. K. Tan, A. Kovács, S. Blügel, R. E. Dunin-Borkowski, *Ultramicroscopy* **2021**, *220*, 113155.
[31] S. A. Montoya, S. Couture, J. J. Chess, J. C. T. Lee, N. Kent, D. Henze, S. K. Sinha, M. Y. Im, S. D. Kevan, P. Fischer, B. J. McMorran, V. Lomakin, S. Roy, E. E. Fullerton, *Phys. Rev. B* **2017**, *95*, 024415.
[32] B. Wang, P. K. Wu, N. Bagués Salguero, Q. Zheng, J. Yan, M. Randeria, D. W. McComb, *ACS Nano* **2021**, *15*, 13495.
[33] S. Hayami, Y. Motome, *Phys. Rev. Lett.* **2018**, *121*, 137202.
[34] F. Ajejas, Y. Sassi, W. Legrand, S. Collin, J. P. Garcia, A. Thiaville, S. Pizzini, N. Reyren, V. Cros, A. Fert, *Phys. Rev. Mater.* **2022**, *6*, L071401.
[35] W. Legrand, D. Maccariello, N. Reyren, K. Garcia, C. Moutafis, C. Moreau-Luchaire, S. Collin, K. Bouzehouane, V. Cros, A. Fert, *Nano Lett.* **2017**, *17*, 2703.
[36] S.-G. Je, P. Vallobra, T. Srivastava, J.-C. Rojas-Sánchez, T. H. Pham, M. Hehn, G. Malinowski, C. Baraduc, S. Auffret, G. Gaudin, S. Mangin, H. Béa, O. Boulle, *Nano Lett.* **2018**, *18*, 7362.
[37] Z. Wang, M. Guo, H.-A. Zhou, L. Zhao, T. Xu, R. Tomasello, H. Bai, Y. Dong, S.-G. Je, W. Chao, H.-S. Han, S. Lee, K.-S. Lee, Y. Yao, W. Han, C. Song, H. Wu, M. Carpentieri, G. Finocchio, M.-Y. Im, S.-Z. Lin, W. Jiang, *Nat. Electron.* **2020**, *3*, 672.
[38] C. Liu, J. Jiang, C. Zhang, Q. Wang, H. Zhang, D. Zheng, Y. Li, Y. Ma, H. Algaidi, X. Gao, Z. Hou, W. Mi, J. Liu, Z. Qiu, X. Zhang, *Adv. Sci.* **2023**, *10*, 2303443.
[39] S. Schlotter, P. Agrawal, G. S. Beach, *Appl. Phys. Lett.* **2018**, *113*, 092402.
[40] Z. Wang, M. Guo, H. A. Zhou, L. Zhao, T. Xu, R. Tomasello, H. Bai, Y. Dong, S. G. Je, W. Chao, H. S. Han, S. Lee, K. S. Lee, Y. Yao, W. Han, C. Song, H. Wu, M. Carpentieri, G. Finocchio, M. Y. Im, S. Z. Lin, W. Jiang, *Nat. Electron.* **2020**, *3*, 672.
[41] A. Vansteenkiste, J. Leliaert, M. Dvornik, M. Helsen, F. Garcia-Sanchez, B. Van Waeyenberge, *AIP Adv.* **2014**, *4*, 107133.
[42] R. Cheng, M. Li, A. Sapkota, A. Rai, A. Pokhrel, T. Mewes, C. Mewes, D. Xiao, M. De Graef, V. Sokalski, *Phys. Rev. B* **2019**, *99*, 184412.
[43] I. Lemesh, G. S. D. Beach, *Phys. Rev. B* **2018**, *98*, 104402.
[44] S. A. Montoya, S. Couture, J. J. Chess, J. C. T. Lee, N. Kent, D. Henze, S. K. Sinha, M. Y. Im, S. D. Kevan, P. Fischer, B. J. McMorran, V. Lomakin, S. Roy, E. E. Fullerton, *Phys. Rev. B* **2017**, *95*, 024415.
[45] R. D. Desautels, L. DeBeer-Schmitt, S. A. Montoya, J. A. Borchers, S.-G. Je, N. Tang, M.-Y. Im, M. R. Fitzsimmons, E. E. Fullerton, D. A. Gilbert, *Phys. Rev. Mater.* **2019**, *3*, 104406.
[46] M. D. DeJong, K. L. Livesey, *Phys. Rev. B* **2015**, *92*, 214420.
[47] B. Wang, D. W. McComb, *Ultramicroscopy* **2023**, *245*, 113665.
[48] A. R. C. McCray, T. Cote, Y. Li, A. K. Petford-Long, C. Phatak, *Phys. Rev. Appl.* **2021**, *15*, 044025.